Journal of Materials Science & Technology 107 (2022) 172–182

Contents lists available at ScienceDirect

Journal of Materials Science & Technology

journal homepage: www.elsevier.com/locate/jmst

Research Article

Tailoring the microstructure, mechanical and tribocorrosion performance of (CrNbTiAlV)N_x high-entropy nitride films by controlling nitrogen flow

Cunxiu Zhang[a,b], Xiaolong Lu[a,d], Cong Wang[a,c], Xudong Sui[a,c,d,*], Yanfang Wang[b], Haibin Zhou[a,d], Junying Hao[a,c,*]

[a] State Key Laboratory of Solid Lubrication, Lanzhou Institute of Chemical Physics, Chinese Academy of Sciences, Lanzhou 730000, China
[b] School of Materials Science and Engineering, China University of Petroleum (East China), Qingdao 266580, China
[c] Center of Materials Science and Optoelectronics Engineering, University of Chinese Academy of Sciences, Beijing 100049, China
[d] Qingdao Center of Resource Chemistry and New Materials, Qingdao 266000, China

ARTICLE INFO

Article history:
Received 11 June 2021
Revised 23 July 2021
Accepted 6 August 2021
Available online 14 October 2021

Keywords:
High-entropy nitride films
Nitrogen flow
Tribocorrosion performance
Magnetron sputtering

ABSTRACT

The (CrNbTiAlV)N_x high-entropy nitride films were fabricated by adjusting nitrogen flow via magnetron sputtering. The microstructure, mechanical, electrochemical and tribocorrosion performances of the films were studied. The results show that the films transform from amorphous to nanocrystalline structure as nitrogen flow increased. The nanocrystalline films show super hardness (> 40 GPa) and adhesion strength (> 50 N). The amorphous film has a pretty anti-corrosion in static corrosion, while not in tribocorrosion condition. The film deposited at nitrogen flow of 38 sccm exhibits the optimal tribocorrosion performance in artificial seawater, with the highest open circuit potential (~ − 0.1 V vs. Ag/AgCl), the lowest friction coefficient (~ 0.162) and wear rate (~ 7.48 × 10^{-7} mm^3 N^{-1} m^{-1}).

1. Introduction

Corrosion has always been a huge challenge faced by mankind when exploring the ocean, which will cause the loss of a large number of metal materials and waste of resources [1,2]. The invention of materials such as stainless steel and titanium alloy has significantly improved this problem, due to their excellent passivation film forming ability [3–6]. However, when these materials are designed as mechanical components and used in seawater environments, the passive film is easily damaged, and then further accelerates corrosion under the coupling of wear and corrosion [7–9]. Thus, surface coating technology is proposed to simultaneously improve the corrosion and tribological properties of mechanical parts. Common coating technologies mainly include organic paints [10,11], spraying [12–14], electroplating [15] and vapor deposition [16]. Among them, the prepared coating via vacuum vapor deposition has a compact structure and good tribological properties, which is suitable for the surface protection of mechanical moving parts in the marine environment [17,18].

Recently, the high-entropy alloy nitride films/coatings (HENFs/HENCs) prepared by vacuum vapor deposition, have become the focus of research, which not only show similar excellent properties with bulk high-entropy alloys (HEAs), but even better than them in some properties [19–24]. Up to date, it has been reported that HENFs have many excellent performances, including anti-corrosion and wear resistance, suggesting a good application prospect in tribocorrosion conditions [25–29]. Chen et al. [30] researched the effect of nitrogen content (R_N) on the electrochemical properties of VAlTiCrMo coatings, and the results showed that the corrosion resistance of the coating was enhanced by the increase of R_N. Hsueh et al. [31] demonstrated that the electrochemical performances of $(AlCrSiTiZr)_{100-x}N_x$ coatings were synergistically affected by substrate bias and nitrogen flow. The mechanical performances in HENFs have also been widely investigated. Feng et al. [32] discovered that the (CrNbTaMoV)N nitride coatings had a lower friction coefficient and wear rate than CrNbTaMoV metallic coatings. Ren et al. [33] investigated that the (AlCrMoZrTi)N nitride films showed better friction and wear performance than (AlCrMoNiTi)N, due to Zr element as a strong nitride forming element.

In this study, considering the strong nitride forming elements [34], five mental elements are selected to synthesize (CrNbTiAlV)N

* Corresponding authors.
E-mail addresses: suixudong@licp.cas.cn (X. Sui), jyhao@licp.cas.cn (J. Hao).

https://doi.org/10.1016/j.jmst.2021.08.032
1005-0302/

Table 1
The details of the process parameters.

Process parameters	Pre-cleaning	Deposited films					
		Cr	HEFNs				
Current (A)	0.4	4.5	4.5	4.5	4.5	4.5	4.5
N_2 flow (sccm)	0	0	0	8	18	38	58
Ar flow (sccm)	18	18	18	18	18	18	18
Working Pressure (Torr)	2.5×10^{-3}	2.5×10^{-3}	2.5×10^{-3}	2.6×10^{-3}	3.2×10^{-3}	4.1×10^{-3}	5.1×10^{-3}
Bias (V)	− 450	− 60	− 126	− 126	− 126	− 126	− 126
Time (min)	30	8	240	240	240	240	240

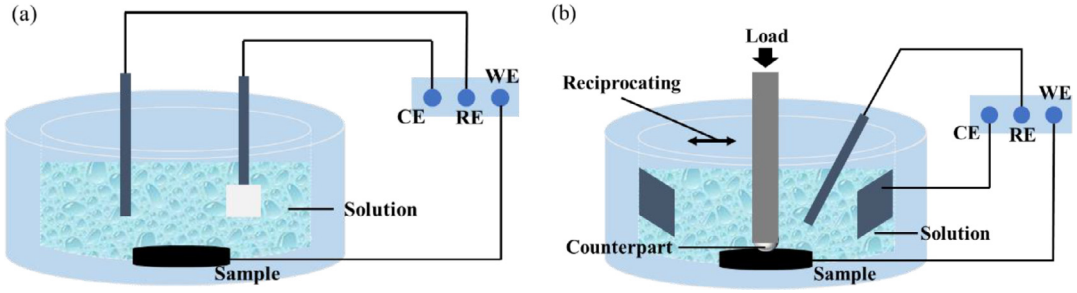

Fig. 1. Schematic diagram of (a) static electrochemical test setup and (b) the reciprocating tribocorrosion device.

films, in the expectation of obtaining good mechanical and tribological property. Meanwhile, the doping Cr, Ti and Al elements can promote the formation of passivation film, which is helpful for improving its anti-corrosion. However, there is little research on the anti-corrosion and wear resistance of (CrNbTiAlV)N_x films. Moreover, previous reports mostly focused on the single wear or corrosion property, and few studied the tribocorrosion coupling behavior of the HENFs. Therefore, (CrNbTiAlV)N_x films are fabricated using Cr-Nb-Ti-Al-V splicing target via magnetron sputtering (MS) method. The microstructure, mechanical and tribological performances of films are tuned via changing nitrogen flow. The influencing factors of the (CrNbTiAlV)N_x films in static electrochemical and dynamic tribocorrosion conditions are discussed.

2. Experimental details

2.1. Film deposition

The (CrNbTiAlV)N_x films were successfully fabricated on AISI 440 C steel (high-carbon high chromium martensitic stainless, with a size of Φ 25 mm × 4 mm) and silicon wafer (20 mm × 20 mm) substrates using MS method. Two kinds of sputtering targets, pure Cr and CrNbTiAlV splicing target were applied. To remove oil stain and impurities, all substrates were successively cleaned by ultrasonic in petroleum ether and ethanol for ~15 min. After then, the substrates were fixed on a rotated holder. When the pressure of the vacuum chamber is lower than 3×10^{-5} Torr, the process can be operated. Before deposition of the films, the low-energy Ar^+ ion bombardment was applied to the samples for 30 min to eliminate the oxides. In order to increase the adhesion of the film to the substrate, an interlayer of Cr (~ 150 nm in thickness) was deposited for 8 min. Subsequently, the HEFNs were prepared at 0 sccm, 8 sccm, 18 sccm, 38 sccm and 58 sccm, namely S0, S8, S18, S38, S58, respectively. No additional heating source was provided for the substrate during deposition. The process parameters for preparing the films are shown in Table 1.

2.2. Film characterization

The elemental distribution of (CrNbTiAlV)N_x films was assessed by EDS (UltraDry). Investigating the effect of nitrogen flow rate on the cross-section and surface morphologies of films, FESEM (JSM 7610 F) was used. The GIXRD (Bruker D 8 Advance) was used to detect the crystal structure of films. The grazing incident angle and scanning range were set at 1° and 20° to 80°, respectively. Nano Indenter (Agilent XP) was applied to measure the hardness and Young's modulus of films. Avoiding the adverse impact of the substrate on the measured data as much as possible, the indentation depth was set as 100 nm. A scratch tester (MFT 4000, China) was applied to evaluate the adhesion between film to substrate. The loading rate and the termination load are 80 N/min and 100 N, respectively. The surface curvature of films was investigated by the film stress tester (FST 1000), and converted to residual stress σ via the Stoney equation:

$$\sigma = \frac{E}{1-\nu}\frac{t^2}{6d}\left(\frac{1}{R_2}-\frac{1}{R_1}\right) \quad (1)$$

where ν and E are referred to the Poisson ratio and Young's modulus of the AISI 440 C steel, respectively. t and d are defined as the thickness of the substrate and film in turn. R_1 and R_2 are the curvatures of substrate and film in order.

2.3. Corrosion and tribo-corrosion tests

The corrosion tests of (CrNbTiAlV)N_x films were performed in artificial seawater at room temperature using the electrochemical station (CS 350, China). The artificial seawater is simulated by 3.5 wt.% NaCl solution. The diagram of the static electrochemical setup is shown in Fig. 1(a). In this diagram, the saturated calomel electrode (SCE) is connected to the reference electrode (RE) terminal and the platinum sheet (Pt) is connected to the counter electrode (CE) terminal. The experimental sample is acted as the working electrode (WE). In the subsequent polarization measurement, the electrode area, potential scanning range and speed were set as 1 cm^2, − 0.6 V to + 1.2 V (vs. OCP) and 1 mV/s, respectively. Fig. 1(b) shows the schematic diagram of the tribocorrosion device (MFT−EC 4000, China). The electrochemical system was composed of a saturated Ag/AgCl, a graphite and the film sample. The Al_2O_3 ball (Φ 6 mm) was acted as the friction pair. The applied load, the sliding frequency and the unidirectional slide length were 5 N, 0.1 Hz and 5 mm, respectively. The evolution of OCP and friction value were recorded for 50 min. The tribo-corrosion test was divided into three stages, including soaking for 10 min, sliding for

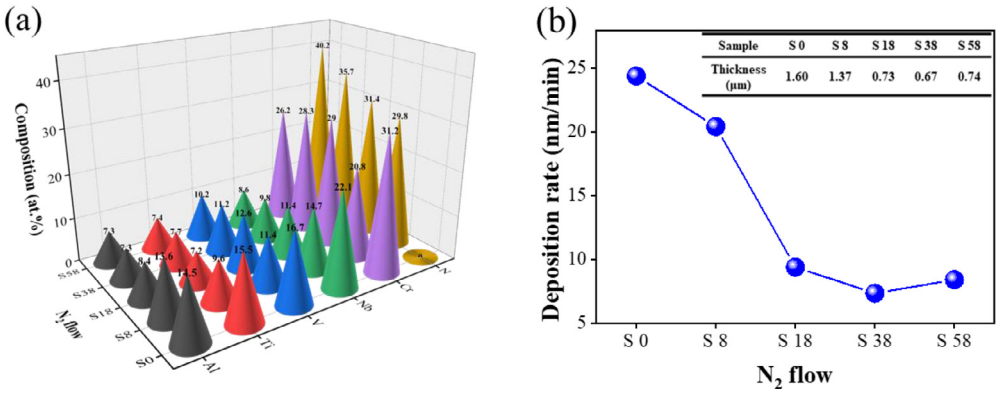

Fig. 2. Element compositions (a), and deposition rate (b) of the (CrNbTiAlV)N_x high-entropy films as a function of N_2 flow.

30 min, and passivation for 10 min. The 3D profiles of wear track and wear volume loss were obtained using the three-dimensional profiler (MicroXAM 800, America). The FESEM and EDS were utilized to measure the wear morphologies and elements distribution. All the corrosion and tribo-corrosion tests were conducted at least twice for confirming the repeatability. The wear rate (W_R) is defined as the volume worn per unit load per unit length and its calculation formula is as follows:

$$W_R = \frac{V_T}{N \cdot L} \tag{2}$$

where V_T is the total volume loss, N and L are the applied load and total sliding distance, respectively.

3. Results and discussions

3.1. Element compositions and deposition rate analysis

Fig. 2(a) depicts the elemental composition of (CrNbTiAlV)N_x films. Clearly, as for CrNbTiAlV metallic film, the concentration of Cr, Nb, Ti, Al and V is 31.2 at.%, 22.1 at.%, 14.5 at.%, 16.7 at.%, and 15.5 at.%, respectively. Although the composition of five metal elements is different, all of them are within the scope of 5 at.% – 35 at.%. In other words, it is doable to fabricate high-entropy films. The nitrogen content of nitride films increases and reaches 40.2 at.% at nitrogen flow of 58 sccm. In addition, it should be particularly pointed out that the content of Cr among metal elements is high, which may be attributed to its high sputtering rate and strong binding ability with nitrogen [35,36]. Fig. 2(b) displays the change in deposition rate of (CrNbTiAlV)N_x films as nitrogen flow. It is observed that there is a decrease in deposition rate from 24.39 nm/min of S0 to 7.35 nm/min of S38. According to previous studies [28,30], the reason for the decrease of deposition rate with the increased nitrogen flow can be explained from the following two perspectives. On the one hand, as the nitrogen flow increases, the probability of collisions between argon ions and nitrogen molecules in the process of bombarding the target material increases, resulting in a decrease in the energy of the argon ions, thereby reducing the deposition rate of the film. Another possible reason is that some nitrides are formed on the target surface, especially in high nitrogen flow, which will hinder the sputtering of metal elements. This phenomenon is also vividly known as “target poisoning”.

3.2. Microstructure and phase formation analysis

Fig. 3 presents the cross-sectional and surface morphologies of (CrNbTiAlV)N_x films. The smooth surface and dense cross-sectional morphology, as shown in Fig. 3(a) and (f), are observed in CrNbTiAlV high-entropy metallic film, which is similar to the amorphous structure. With the addition of nitrogen, the deposited film gradually changes into a typical columnar structure (Fig. 3(g, h)). Meanwhile, the surface particles gradually transform from sharp (Fig. 3(b, c)) to dome (Fig. 3(d, e)), which may be related to the competitive growth of crystals [37]. As seen from Fig. 3(k), the thickness of Cr interlayer is about 150 nm. There is a decrease in the film thickness as increasing nitrogen flow. S38 has a denser structure with a minimum thickness of 0.67 μm (Fig. 3(i)). The thickness of the film is proportional to the deposition rate. With the increase of nitrogen flow, the decrease of the film thickness is mainly attributed to the continuous decrease of argon ions energy and target poisoning discussed above.

Fig. 4 shows the XRD patterns of (CrNbTiAlV)N_x high-entropy films deposited under different nitrogen flows. S0 sample has a broadly diffuse scattering peak in the range of 35° – 45°, indicating the existence of an amorphous phase. With the addition of nitrogen flow, the diffraction peaks of (111), (200), (220), (311) belonged to face-centered cubic (fcc) structure are displayed in the XRD diagram. The (111) preferred orientation is detected in (CrNbTiAlV)N nitride films, which is consistent with the results of most high-entropy nitride films reported, such as (VAlTiCrMo)N, (AlCrMoTaTi)N and (AlCrTaTiZr)N [30,38,39]. For the fcc structure, (111) is the optimal densely arranged plane with the lowest strain energy, which is conducive to the formation of (111) preferred orientation in competitive growth. Besides, the diffusion of metal atoms on (111) is much more difficult than that of (200), because (111) has three N backbonds of metal compared to one of (200) [40]. Therefore, all the nitride films show a (111) preferred orientation.

Clearly seen that the intensity of the diffraction peaks, especially (111) plane, is significantly changed by nitrogen flow. The films deposited under low nitrogen flow (e.g., S8, S18) have a high intensity of diffraction peaks, while the films at high nitrogen flow (e.g., S38, S58) show a lower intensity. A high deposition rate at low nitrogen flow promotes the rapid growth of grains, thus showing a strong diffraction peak in the XRD pattern. The increase in lattice distortion and grain refinement under high nitrogen flow are considered as the main reasons for the weakening of diffraction peak [41]. Table 2 lists the relative intensity of diffraction peaks and average grain sizes of (CrNbTiAlV)N films. The largest lattice constant of 4.32233 Å and the smallest grain size of 11.74 nm are measured to S38, resulting in a maximum weakening effect. Therefore, S38 has a lower intensity of diffraction peaks.

Additionally, only fcc structure is observed in the XRD pattern, implying that the solid solution structure instead of intermetallic compound is easily obtained in HEFNs, which is consistent with

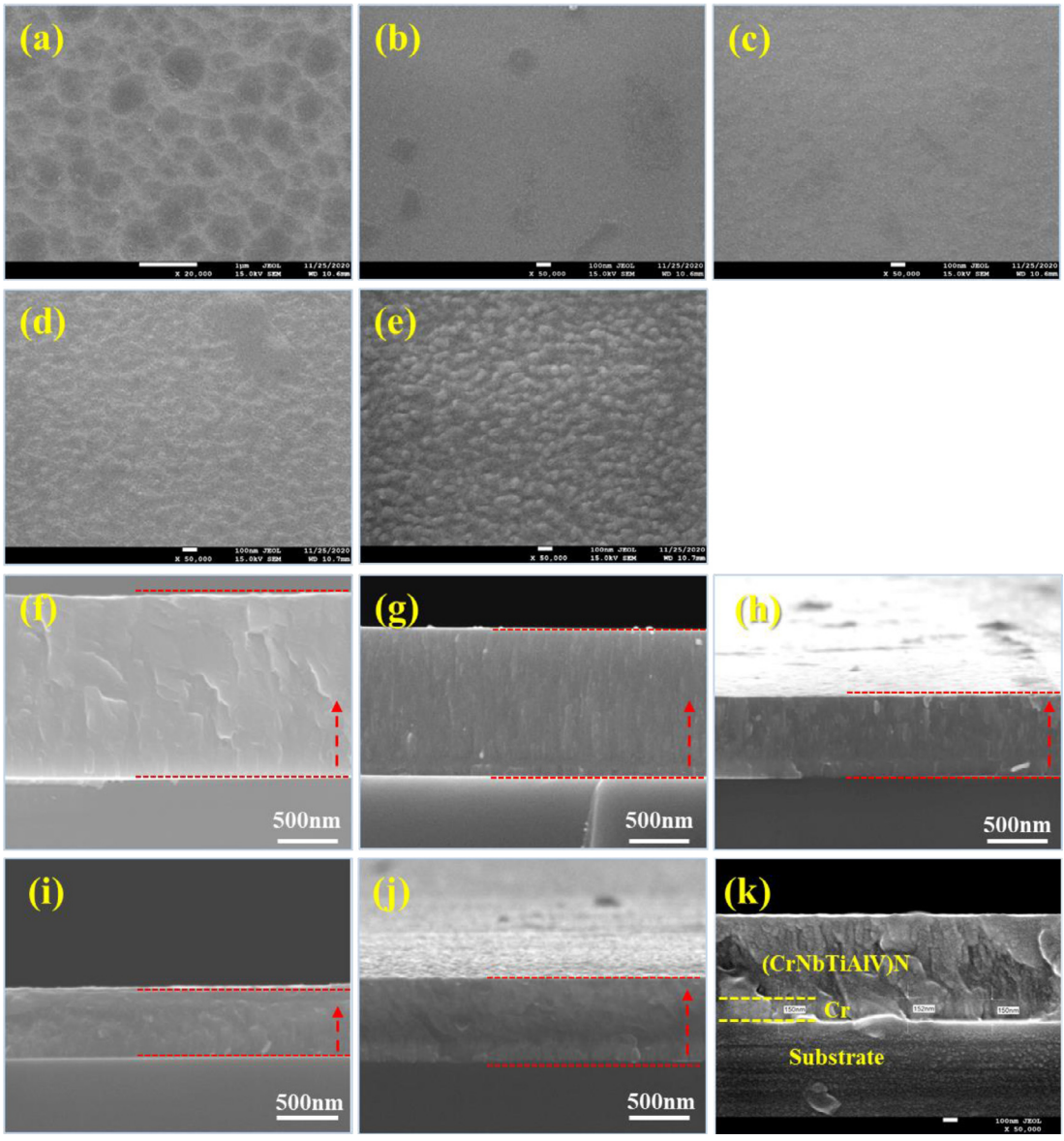

Fig. 3. SEM cross-section and surface morphology of (CrNbTiAlV)N_x high-entropy films deposited under different nitrogen flows: (a, f) S0; (b, g) S8; (c, h) S18; (d, i) S38; (e, j) S58; (k) high magnification SEM image of S38 (in order to improve the resolution of the image, the sample was sprayed with gold for 60 s in advance).

Table 2
Relative intensity of diffraction peaks, average grain sizes and lattice constant of (CrNbTiAlV)N_x films.

Sample	Relative intensity				Average grain size (nm)	Lattice constant (Å)
	(111)	(200)	(220)	(311)		
S8	216	41	24	5	12.41	4.26015
S18	680	152	182	28	14.05	4.31748
S38	25	5	7	–	11.74	4.32233
S58	114	8	35	9	13.30	4.30363

the phase formation of HEAs [42]. The atomic radius difference (δ) and the mixing entropy (ΔS_{mix}) of multi-principal systems are determined by the following formulas:

$$\delta = \sqrt{\sum_{i=1}^{n} c_i\left(1 - r_i/\bar{r}\right)^2} \tag{3}$$

$$\Delta S_{mix} = -R\sum_{i=1}^{n} c_i Ln c_i \tag{4}$$

where r_i was the atomic radius, c_i was the atomic ratio of the element, $\bar{r} = \sum_{i=1}^{n} c_i r_i$ was the average atomic radius, and R is the gas constant (8.314 J mol^{-1} K^{-1}). Table 3 presents the atomic radius of each element. The values of ΔS_{mix} and δ of (CrNbTiAlV)N_x deposited at different nitrogen flows are listed in Table 4. As for the sample S0, the ΔS_{mix} is 13.01 kJ mol^{-1} ($\geq 1.5R$), corresponding to the definition of high entropy alloy proposed by Yeh et al. [43]. At present, there is no systematic explanation about the formation phase of high-entropy thin films. But according to Zhang's

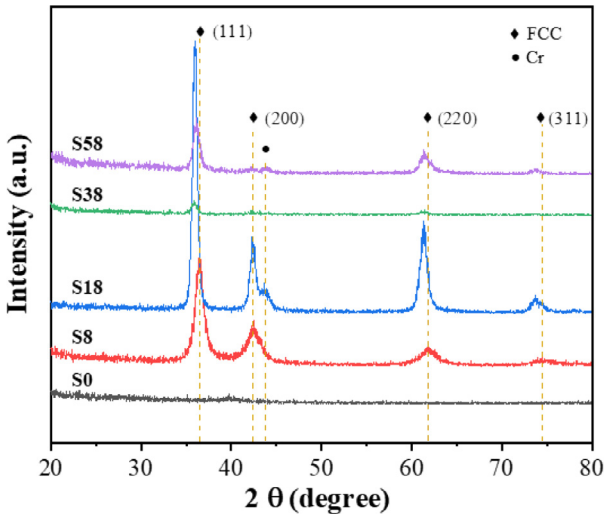

Fig. 4. XRD patterns of (CrNbTiAlV)N_x films deposited under different nitrogen flows.

Table 3
The radius of elements in (CrNbTiAlV)N_x system.

Element	Cr	Nb	Ti	Al	V	N
Radius(pm)	124.9	142.9	146.2	143.2	131.6	75

Table 4
The nitrogen content, δ and ΔS_{mix} value of the (CrNbTiAlV)N_x high-entropy films at different N_2 flows.

N_2 flow	N content (at.%)	δ (%)	ΔS_{mix} (kJ mol^{-1})
S0	0	6.41	13.01
S8	29.8	24.42	11.25
S18	31.4	24.51	10.52
S38	35.7	25.64	10.13
S58	40.9	27.04	9.88

study [44], it has been reported that the δ forming fcc structure is about 23% in $(Al_{0.5}CrFeNiTi_{0.25})N_x$ nitride films. In our study, the value δ of FCC phase formed in (CrNbTiAlV)N system is similar to the results mentioned above.

3.3. Mechanical performances of the films

Fig. 5(a) depicts the change in residual stress (σ) of (CrNbTiAlV)N_x high entropy films at different nitrogen flows. Clearly seen that all the films present compressive stress. Among them, the CrNbTiAlV metallic film has the lowest σ of – 2.35 GPa. Following as the increasing nitrogen flow, the σ elevates continuously and peaks at 38 sccm with a maximum value of – 6.55 GPa. The variation in σ is considered to be caused by the increase of nitrogen and the effect of ion bombardment during deposition [41]. Fig. 5(b) describes the evolution in hardness and modulus of (CrNbTiAlV)N_x films. The hardness of CrNbTiAlV metallic film is around 17.46 GPa, which is relatively higher than some bulk HEAs, due to its amorphous structure without dislocations for slipping [41]. Subsequently, the hardness of films is enhanced obviously with the increasing nitrogen flow, and peaks the maximum value of 49.95 GPa at 38 sccm.

The grain size decreases and the lattice constant increases with the increase of nitrogen flow. As shown in Table 2, S38 has the smallest grain size of 11.74 nm and the largest lattice constant of 4.32233 Å. The grain refinement and lattice distortion effect will synergistically improve the hardness of S38. In addition, from the perspective of magnetron sputtering film [45,46], the residual compressive stress caused by ion bombardment can also enhance its mechanical properties, namely defect hardening. S38 has the maximum residual compressive stress of –6.55 GPa (Fig. 5(a)), promoting a more compact structure (Fig. 3(i)). Based on the above analysis, the effect of solid-solution strengthening, finer grain-size strengthening, residual compressive stress and compact structure hardening can synergistically enhance the hardness of S38. Therefore, S38 has the highest hardness. However, the hardness of the film decreases when the nitrogen flow is further increased to 58 sccm, indicating the deterioration of mechanical properties. This decrease may be attributed to the decrease in residual compressive stress, the formation of loose structures, as well as the increase in grain size under high nitrogen flow.

Fig. 5(c) depicts the load–displacement curves of films fabricated at various nitrogen flows. All curves are divided into two parts, namely plastic deformation area and elastic recovery area, which are respectively marked in the figure. Compared with the S0 sample, the other samples have a narrower plastic deformation area, which means that the nitride films own better resistance to plastic deformation. The doping of nitrogen increases the hardness and shear strength of film, thus improving its deformation resistance. Fig. 5(d) shows the H/E and H^3/E^2 ratio of the films at different nitrogen flows. S38 sample has the highest H/E value of 0.13 and H^3/E^2 of 0.88, possibly attributed to its compact microstructure. The ratio of H/E is defined as the energy absorbed by the film before failure, and the H^3/E^2 is an index that characterizes the ability of the film to resist plastic deformation [47,48]. A high value of H/E is usually expected to have good cracking resistance and excellent wear resistance. This prediction will be validated in the following tests.

Fig. 6(g) presents the scratch morphologies of (CrNbTiAlV)N_x films prepared at different nitrogen flows. It can be seen that two failure methods are recognized, which refer to the appearance of circumferential crack (labeled as L_{C1}) and the exposure of substrate (labeled as L_{C2}), respectively. The L_{C1} and L_{C2} of experimental films are marked in Fig. 6(a-e). The worn-through resistance of the film is related to the value of L_{C2}, which is defined as the adhesion strength of the film. Fig. 6(f) shows the adhesion L_{C2} of experimental films. S0 sample has the lowest L_{C2} of 24.95 N, while S18 sample possesses the highest L_{C2} of 71 N, indicating that the adhesion strength of the film to substrate is improved obviously by nitriding. As shown in Fig. 6(g), no significant signature of L_{C1} is observed, and a large area spalling of the film is formed under continuous load (zone marked as a and b in S0 sample). With increasing nitrogen flow to 8 sccm, the L_{C2} greatly goes up to 54.15 N. However, the wide circumferential cracks and severe transverse propagation are shown in zone c of S8, while some brittle peelings are formed on the scratch edges of zone d. This is mainly due to the increase in hardness and brittleness of the film after nitriding. For S18 sample, only tiny circumferential cracks are observed such as zone e, and no obviously brittle spalling appears on the scratch edges, implying that the crack propagation can be effectively restrained with an appropriate nitrogen flow. Actually, excessive residual stress will lead to a decrease in the adhesion of the film. As the further increment of nitrogen flow, the slight propagation and brittle spalling appear again in S38 and S58 samples (marked as zone f, h, g and i). Meanwhile, the adhesion strength decreases somewhat. Even so, as shown in Fig. 6(f), the L_c value of S38 is still at a high value of about 53.35 N.

3.4. Electrochemical performances of the films

The corrosion resistance of substrate and (CrNbTiAlV)N_x films are assessed under static electrochemical measurements. Fig. 7 illustrates the polarization curves of the substrate and (CrNbTiAlV)N_x films at different nitrogen flows. The fitted param-

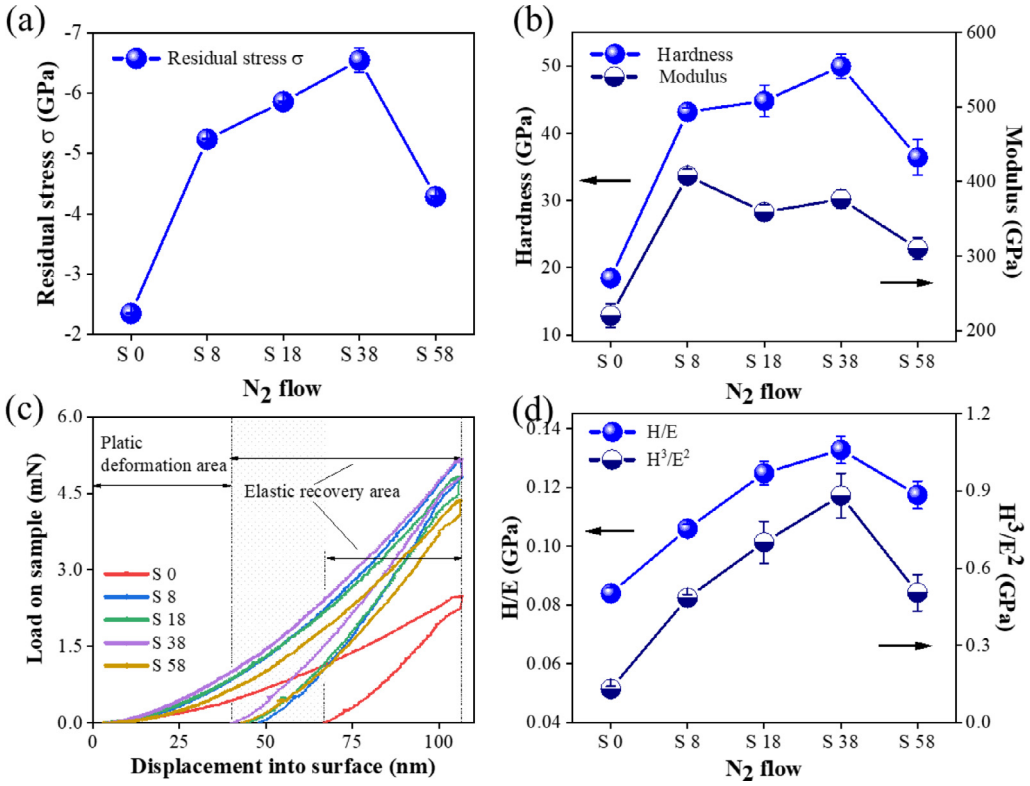

Fig. 5. The residual stress (a), hardness and elastic modulus (b), load–displacement curves (c) and H/E and H^3/E^2 (d) of (CrNbTiAlV)N_x films deposited under different nitrogen flows.

Table 5
The electrochemical parameters fitted from the polarization curve by Cview software.

Sample	E_{corr} (V_{SCE})	E_{pit} (V_{SCE})	i_{corr} ($\mu A/cm^2$)	R_{corr} ($\mu m/PY$)
S0	−0.344	0.833	0.038	0.44
S8	−0.227	–	0.019	0.23
S18	−0.509	0.666	0.344	4.05
S38	−0.091	–	0.015	0.18
S58	−0.427	0.811	0.271	3.19
Substrate	−0.597	0.423	0.337	3.96

eters are collected in Table 5, including corrosion potential (E_{corr}), corrosion current density (i_{corr}), pitting potential (E_{pit}) and corrosion rate (R_{corr}). Generally, the higher E_{corr} and smaller i_{corr} suggest a better corrosion resistance [49]. Compared with the substrate, all the films show a more positive E_{corr}, which indicate a lower corrosion tendency. For S0 sample, its uniform amorphous structure can slow down the penetration of chloride ions, thereby improving its corrosion resistance [50,51]. But pitting occurs at higher anodic polarization potential. The texture of the film is transformed into a columnar structure (such as Fig. 4(h)) at low nitrogen. The introduction of grain boundaries will provide a fast channel for chloride ion diffusion and accelerate corrosion to a certain extent. But, the introduction of nitrogen also increases the chemical inertness of film and improves its corrosion resistance [52]. Thus, when the high-entropy film is properly nitride (such as S38) and has a dense nanocrystalline structure, it is expected to have the best electrochemical performance. As shown in Table 5, the pitting potentials increase from 0.423 V of the substrate to 0.833 V of S0, and no pitting potential is observed for S8 and S38 in the same range of potentiometric scanning, implying their excellent resistance to the penetration and pitting of Cl^-. Furthermore, the value of i_{corr} shows a reduction from 0.344 $\mu A/cm^2$ of S18 to 0.015 $\mu A/cm^2$ of S38, suggesting that the S38 is supposed to own the best corrosion resistance.

3.5. Tribocorrosion performances of the films

Generally, the change of OCP will offer the qualitative feature of electrochemical reactivity on film surface [53,54]. The variation of OCP with testing time in the soaking, sliding, and passivation zone of the substrate and (CrNbTiAlV)N_x films is illustrated in Fig. 8(a) (top). In the soaking area, all the samples show a relatively stable open circuit potential. Moreover, compared with the OCP of other samples, the S0 and S38 possess the higher value of − 0.17 V and − 0.11 V, respectively. As seen in Fig. 8(a), the total sliding process is divided into three zones (I, II and III). When a load of 5 N is applied, the OCP of all these samples shows a downward trend to varying degrees in the initial stage of zone I, which is ascribed to the initial damage in the passive film with the mechanical sliding, and the fresh bare layer with higher reactivity [55,56]. However, two distinct tribocorrosion behaviors are clearly observed for the film with and without nitrogen, respectively. For S0 sample, the sharp drop and fluctuation of OCP are observed in zone I, which is related to its poor mechanical performance. In the subsequent reciprocating friction stage, the passivation film is continuous dissolution and formation, resulting in the ups and downs of OCP in zone II. Eventually, the dissolution and formation rate will reach a dynamic equilibrium [57], thus the relatively stable OCP is obtained in zone III. After the sliding stops, the OCP gradually rises and then stabilizes, corresponding to the re-passivation effect in the absence of the load [58]. In contrast, the OCP of nitride films has only a slight change during the entire sliding process. Due to the doping of nitrogen, the chemical inertness of the film is increased, thus reducing the sensitivity of wear to OCP. Fig. 8(c) shows the enlarged view of OCP and COF changes for S58 and the substrate. It can be seen that when loading (such as Fig. 8(c-1)),

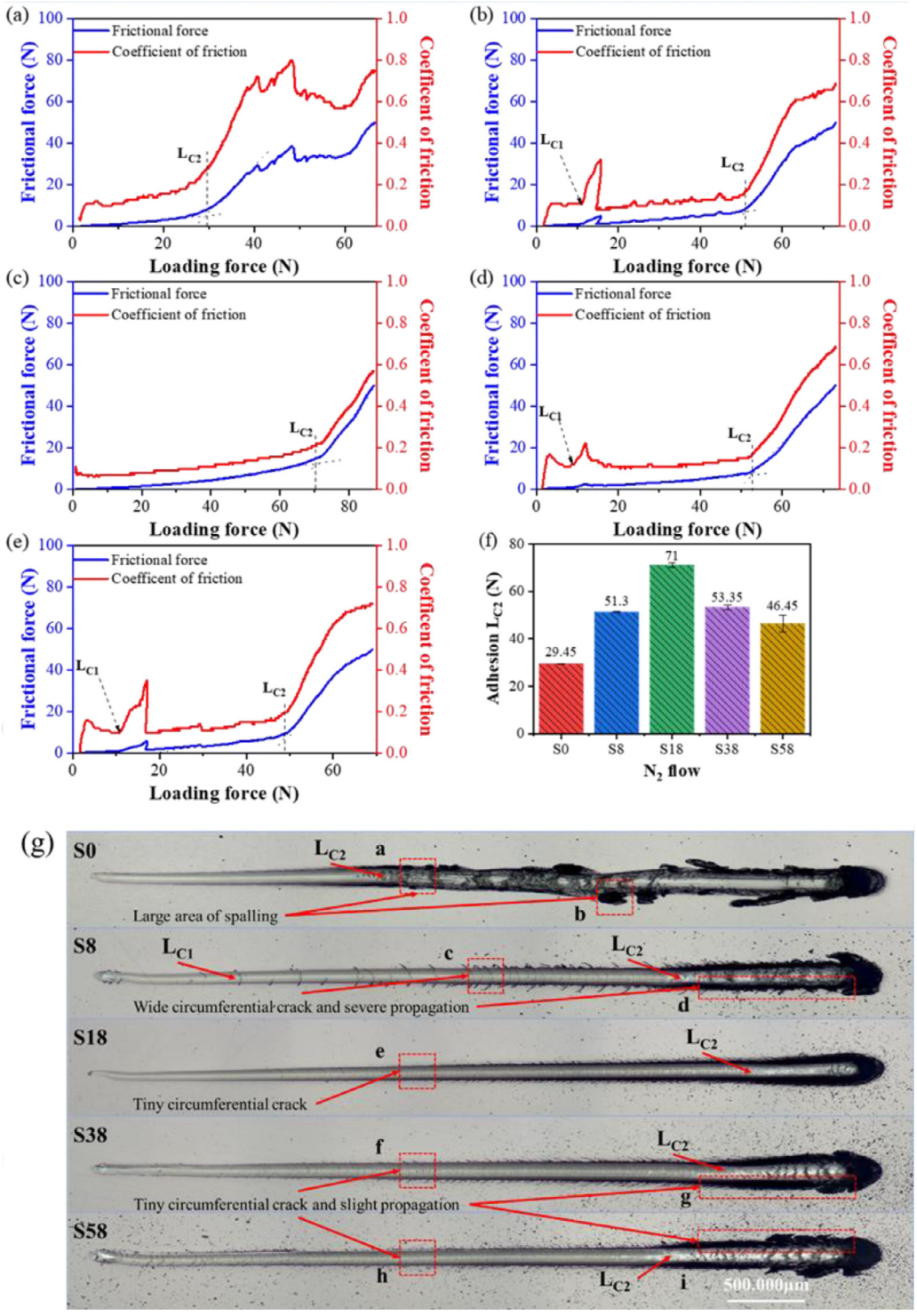

Fig. 6. The experimental curves (a: S0, b: S8, c: S18, d: S38, e: S58), adhesion L_{C2} (f) and scratch morphologies (g) of (CrNbTiAlV)N_x high-entropy films deposited under different nitrogen flows using a scratch tester with a diamond indenter (loading rate and termination load are 80 N/min and 100 N, respectively).

the friction coefficient of substrate and nitride film samples gradually increases, and OCP decreases, and the fluctuation of the former OCP is larger. When the friction coefficient is stable (such as Fig. 8(c-2)), the OCP of the nitride film is more stable than that of the substrate. When unloading (such as Fig. 8(c-3)), the COFs both gradually tend to zero. Compared to the substrate where OCP gradually rises, the OCP of nitride film remains stable, which may be attributed to the surface chemical inertness. In a word, the surface chemical state of the nitride film is better than that of the substrate.

Fig. 8(a) (bottom) represents the COFs of the substrate and (CrNbTiAlV)N_x films during tribocorrosion tests in artificial seawater. The running-in and stabilization period are distinguished in the sliding process. Clearly seen that the COF increases first and then decreases gradually in the running-in stage, which is related to the film's roughness and the contact stress with friction pair. Moreover,

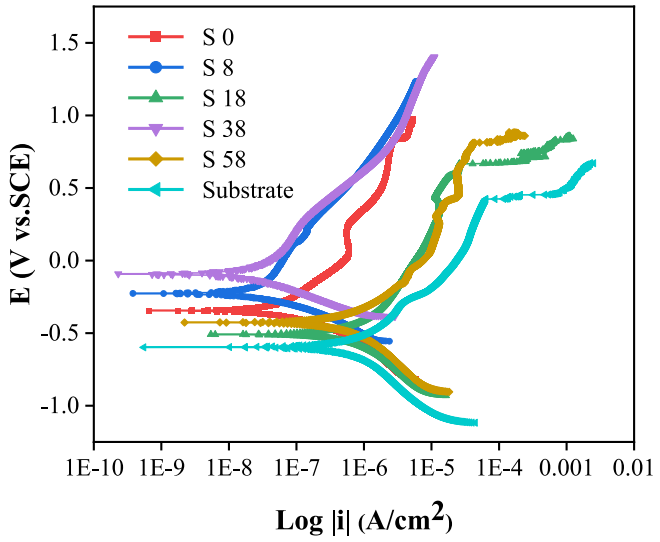

Fig. 7. The potentiodynamic polarization curves of the substrate and (CrNbTiAlV)N_x films at different N_2 flows in artificial seawater at room temperature.

the change of COF is also affected by the surface morphology of wear track [59]. For S0 sample, a violent fluctuation in COF is also observed, which is probably caused by the formation of wear debris accompanying the reciprocating motion [60]. Compared with S0, the nitriding films have a mild friction process. Fig. 8(b) (right axis) records the COF of films under the stable friction stage. Obviously, the S0 has the highest COF of 0.753, which is more than twice that of the substrate, indicating its relatively poor tribocorrosion performance. In contrast, due to the formation of dense microstructure, the COF of the nitride films gradually decreases and reaches the minimum value of 0.162 at 38 sccm.

To further analyze the wear mechanisms of (CrNbTiAlV)N_x high-entropy nitride films, Fig. 9 shows the three-dimensional profiles, SEM and EDS results of wear tracks, respectively. As presented from Fig. 9(a-e), S0 has the widest wear track width of 0.53 mm, followed by the substrate of 0.33 mm. Among the nitride films, S38 shows the smallest wear track width of 0.06 mm. A number of pitting pits appear along the edge of the wear track in Fig. 9(f), resulting in that the substrate obtains a low OCP value in the tribocorrosion test. As listed in Table 6, the EDS result reveals that Cr, Cl, O and Fe elements are found at points 1 and 2. Compared with the substrate, serious furrows and lots of corrosion products are observed across the total surface of wear track for S0. Due to the furrow effect and rough surface, S0 exhibits poor tribological properties, as the friction coefficient increases and fluctuates dramatically. In Fig. 8(b), S0 shows the highest wear rate of 1.78 $\times$ 10^{-4} mm^3 N^{-1} m^{-1}, which is one order of magnitude larger than that of the substrate. Furthermore, a small amount of Fe element is detected at point 3, indicating that the film has been partially worn through. As for the nitride films, the wear rate is significantly reduced because of their improved mechanical properties the addition of nitrogen. Among them, S38 has the lowest wear rate of 7.48 $\times$ 10^{-7} mm^3 N^{-1} m^{-1} (like Fig. 8(b)). S18 and S58 are considered as the film prepared under low and high nitrogen elements, respectively. For S18, the columnar growth texture of the structure may become the diffusion channel of the corrosive media, so some pitting pits appear on the wear track (Fig. 9(h)). Under the action of friction, these pitting pits will be further damaged, or even worn through to the substrate. The Fe element detected in EDS results of point 4 supports this hypothesis. The spallation and corrosion pits are detected on S58 (Fig. 9(j)), which will accelerate the corrosion of the material, showing a decrease in OCP value and an increase in wear rate. In contrast, without obvious corrosion defects are found from SEM image of Fig. 9(i), indicating its excellent tribocorrosion performance in artificial seawater. The compact and smooth surface of wear track can not only hinder the penetration of corrosive media but also keep its friction coefficient at a low value.

Fig. 10 depicts the schematic of the static corrosion and tribocorrosion mechanism of (CrNbTiAlV)N_x high-entropy films under different work environments. As mentioned above, S0 sample has an amorphous structure, and S38 sample presents a compact nanocrystalline structure. In the static corrosion condition, the amorphous structure without grain boundary is favorable for the improved anti-corrosion of film. However, due to the heteroge-

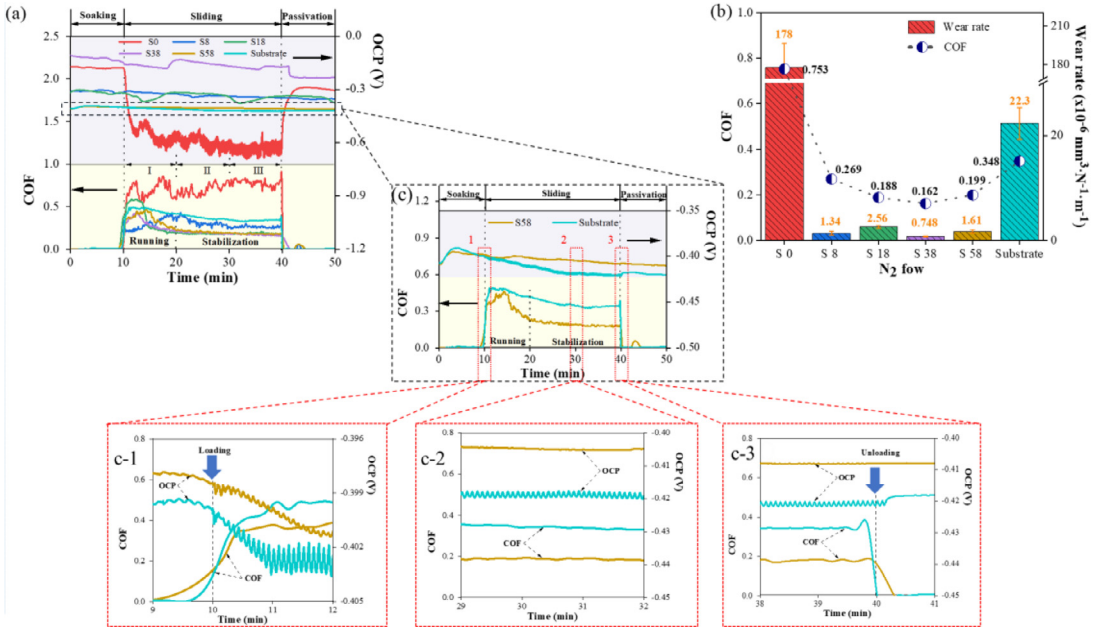

Fig. 8. The evolution of open circuit potential and coefficient of friction in the soaking, sliding, and passivation (a, c), the wear rate and COF (b) of the substrate and (CrNbTiAlV)N_x films in artificial seawater, and the enlarged view of S58 and substrate in loading, stabilizing and unloading stages (c-1, c-2, c-3).

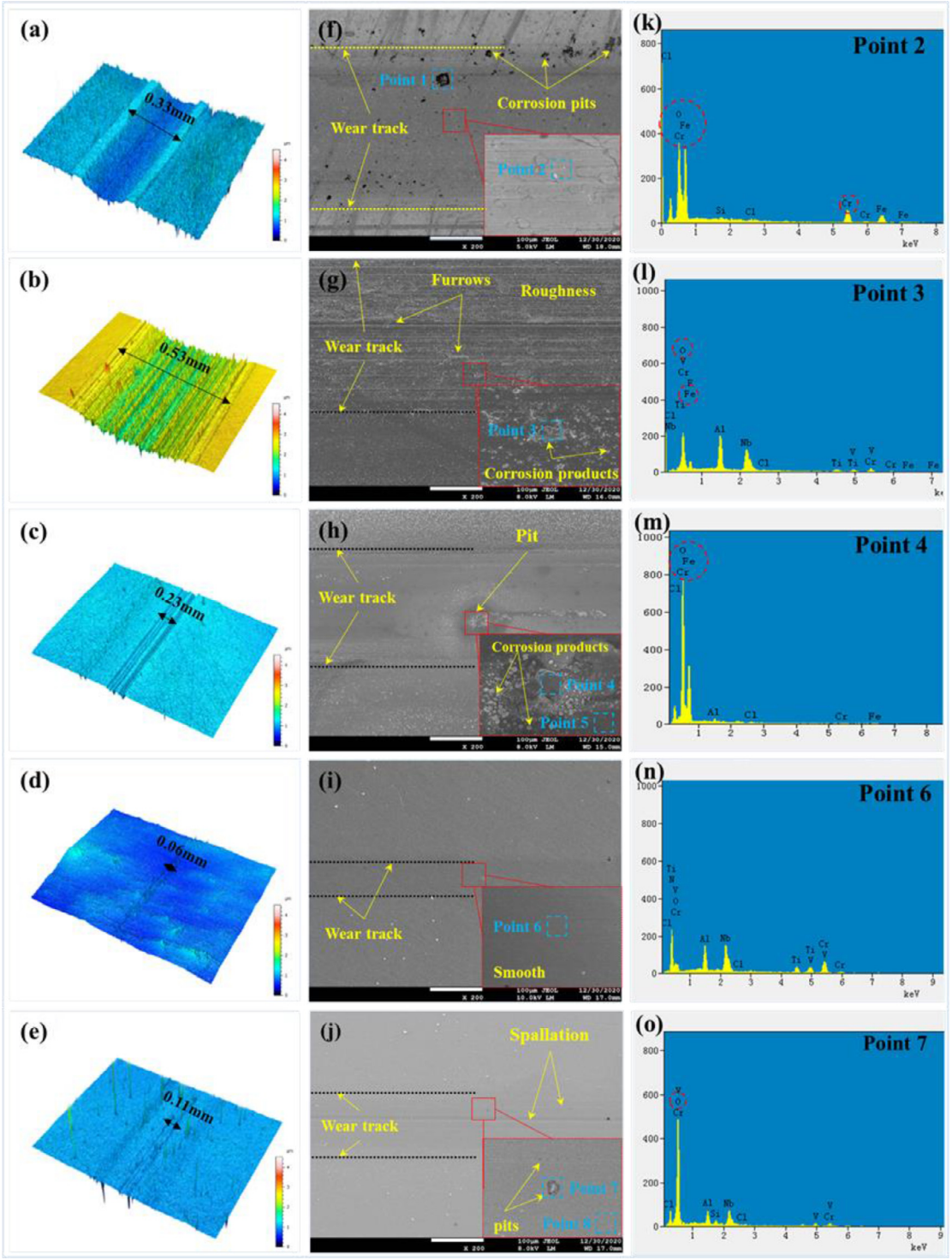

Fig. 9. Three-dimensional profiles, SEM, EDS of wear tracks obtained from the steel substrate (a, f, k) and S0 (b, g, l), S18 (c, h, m), S38 (d, i, n), S58 (e, j, o) films after tribocorrosion test.

neous chemical composition, the electrode surface may have high chemical active sites, which may further form pitting pits under the erosion of chloride ions. Following as nitrogen flow increased, the chemical inertness of S38 sample is significantly enhanced. At the same time, the compact nanocrystalline structure can effectively hinder the penetration of chloride ions. These factors together make S38 sample present a nobler corrosion resistance. The importance of mechanical performances has to be considered under tribocorrosion condition. The amorphous film with poor mechanical properties has a severe material loss and the cracks will provide a fast channel for the diffusion of chloride ions. Meanwhile, the furrows and debris on the wear tracks will increase its COF value. In contrast, S38 sample presents the best comprehensive mechanical properties, such as the highest hardness and excellent adhesion strength. Additionally, the dense and relatively smooth surface not only hinders the penetration of the corrosive media but also makes the friction coefficient quickly stabilize at a low value. With the above analysis, S38 sample with the

Table 6
EDS results of selected points on the wear track after the tribocorrosion tests (at.%).

Sample	Point	Cr	Nb	Ti	Al	V	N	Cl	O	Fe
Substrate	1	24.9	–	–	–	–	–	–	–	75.1
	2	23.4	–	–	–	–	–	0.3	12.7	63.6
S0	3	8.8	12.1	8.4	14.9	3.1	–	1.1	39.9	11.7
S18	4	1.7	–	–	–	–	–	–	21.3	77.0
	5	22.4	9.0	8.3	11.9	1.3	43.7	0.2	3.1	–
S38	6	25.8	9.0	8.1	7.1	9.8	40.2	–	–	–
S58	7	–	7.1	–	4.7	–	–	–	86.5	–
	8	26.6	9.6	6.9	9.6	–	47.3	–	–	–

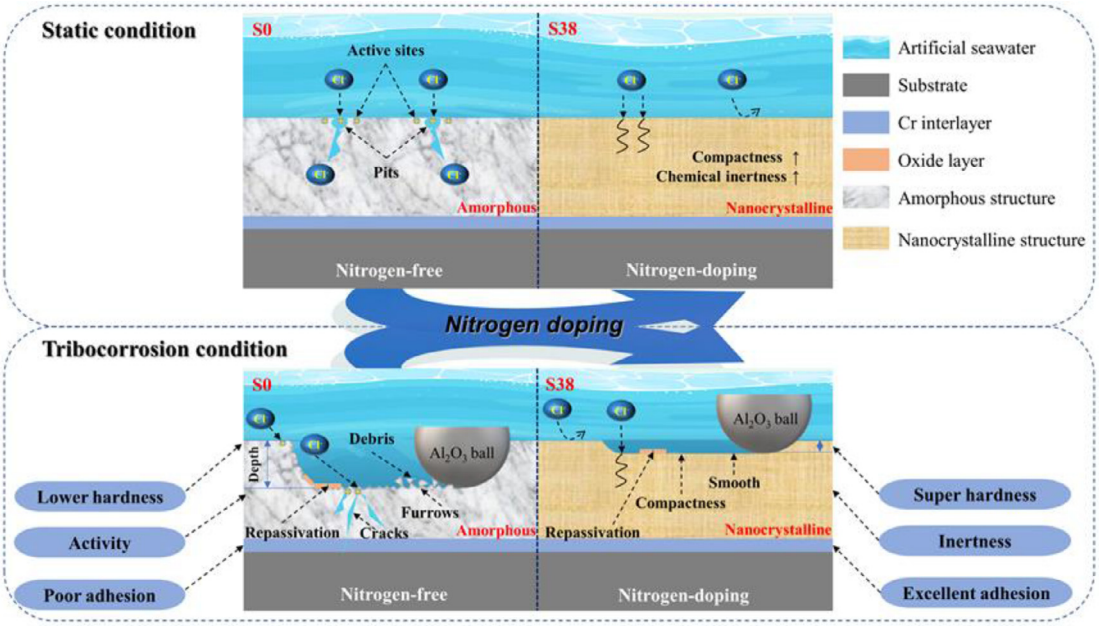

Fig. 10. Schematic of the static corrosion and tribocorrosion mechanism of (CrNbTiAlV)N_x high-entropy films under different work environments.

compact nanocrystalline structure exhibits the best tribocorrosion performance by controlling nitrogen flow.

4. Conclusions

This work aims to tailor the microstructure, mechanical and tribocorrosion performance of (CrNbTiAlV)N_x high-entropy nitride films deposited on AISI 440C steel by controlling nitrogen flow via MS method. Through the microstructure and mechanical properties testing, the reasons for the difference between electrochemical and tribocorrosion behavior of the films under static and dynamic conditions were analyzed. From the experimental results obtained, the main conclusions are as follows:

(1) The CrNbTiAlV high-entropy metallic film has an amorphous structure, while the (CrNbTiAlV)N film has a nanocrystalline structure with the single fcc phase. With the introduction of nitrogen, some nitrides are formed, which have a similar fcc structure. Meanwhile, the mixing of multiple principal elements reduces the free energy and promotes the formation of a simple solid solution.
(2) The mechanical performances of (CrNbTiAlV)N_x films are improved by nitrogen doping. Among these films, S38 has the highest hardness of 49.95 GPa and the largest residual compressive stress of − 6.55 GPa. The scratch testing shows that the nitride film has better adhesion of the film to the substrate. However, the adhesion will deteriorate with excessive residual stress (> − 6 GPa).
(3) In the static condition, the S0 sample exhibits better corrosion resistance compared with the substrate, which is attributed to the fact that the amorphous structure reduces the formation of the corroded microcell. The non-metallicity of the film is improved by the addition of nitrogen. Among nitride films, S38 sample shows the best electrochemical behavior with the most positive E_{corr}, the lowest i_{corr} and the widest passivation region.
(4) In the dynamic condition, the surface chemical state of the film is destroyed with an applied load. Due to the large wear loss, the OCP of the amorphous film has a sharp drop, and the furrow and debris on the wear track surface increase its friction coefficient. In contrast, nitrogen doping reduces the sensitivity of wear to OCP. Nanocrystalline films exhibit smaller wear loss, lower COF and smaller fluctuation of OCP.
(5) In conclusion, the S38 sample has comprehensive mechanical properties, excellent electrochemical and tribocorrosion performance in artificial seawater.

Acknowledgements

The authors gratefully acknowledge the financial support of the National Natural Science Foundation of China (Nos. 51835012 and 51975554), the National Key R&D Plan of China (No. 2018YFB0703803), the program of "Science & Technology International Cooperation Demonstrative Base of Metal Surface Engineering along the Silk Road (No. 2017D01003)" and CAS "Light of West China".

References

[1] K. Rohith, S. Shreyas, K.B. Vishnu Appaiah, R.V. Sheshank, B.B. Ganesha, B. Vinod, Mater. Today: Proc. 18 (2019) 4854–4859.
[2] B.R. Hou, X.G. Li, X.M. Ma, C.W. Du, D.W. Zhang, M. Zheng, W.C. Xu, D.Z. Lu, F.B. Ma, NPJ Mater. Degrad. 1 (2017) 4–13.
[3] S. Jin, A. Atrens, Appl. Phys. A 50 (1990) 287–300.
[4] M. Santamaria, G. Tranchida, F.D. Franco, Corros. Sci. 173 (2020) 108778.
[5] X.J. Yang, C.W. Du, H.X. Wan, Z.Y. Lu, X.G. Li, Appl. Surf. Sci. 458 (2018) 198–209.
[6] J.J. Pang, D.J. Blackwood, Corros. Sci. 105 (2016) 17–24.
[7] X.D. Sui, R.N. Xu, J. Liu, S.T. Zhang, Y. Wu, J. Yang, J.Y. Hao, ACS Appl. Mater. Interfaces 10 (2018) 36531–36539.
[8] H. Kovacı, Y.B. Bozkurt, A.F. Yetim, O. Baran, A. Çelik, Tribol. Int. 156 (2021) 106823.
[9] P.A. Dearnley, B. Mallia, Wear 306 (2013) 263–275.
[10] M.M. Liu, H.X. Hua, Y.G. Zheng, Surf. Coat. Technol. 309 (2017) 579–589.
[11] X.L. Huang, L. Yua, Y.S. Dong, Prog. Org. Coat. 139 (2020) 105446.
[12] A.S.M. Ang, C.C. Berndt, M.L. Sesso, A. Anupam, S. Praveen, R.S. Kottda, B.S. Murty, Metall. Mater. Trans. A 46 (2015) 791–800.
[13] J.K. Xiao, H. Tan, Y.Q. Wu, Surf. Coat. Technol. 385 (2020) 125430.
[14] S. Yin, W. Li, B.O. Song, X.C. Yan, M. Kuang, Y.X. Xu, K. Wen, R. Lupoi, J. Mater. Sci. Technol. 35 (2019) 1003–1007.
[15] Y.L. Li, P. Song, W.Q. Wang, M. Lei, X.W. Li, Mater. Charact. 170 (2020) 110674.
[16] A. Baptista, F.J.G. Silva, J. Porteiro, J.L. Míguez, G. Pinto, L. Fernandes, Proc. Manuf 17 (2018) 746–757.
[17] F. Zhou, Q. Ma, Q.Z. Wang, L.K.Y. Li, J.W. Yan, Tribol. Int. 116 (2017) 19–25.
[18] Y. Wang, J.L. Li, C.Q. Dang, Y.X. Wang, Y.J. Zhu, Tribol. Int. 109 (2017) 285–296.
[19] Y. Zhang, T.T. Zuo, Z. Tang, M.C. Gao, K.A. Dahmen, P.K. Liaw, Z.P. Lu, Prog. Mater. Sci. 61 (2014) 1–93.
[20] X.H. Yan, J.S. Li, W.R. Zhang, Y. Zhang, Mater. Chem. Phys. 210 (2018) 12–19.
[21] Y. Fu, J. Li, H. Luo, C.W. Du, X.G. Li, J. Mater. Sci. Technol. 80 (2021) 217–233.
[22] H. Luo, Z. Li, A.M. Mingers, D. Raabe, Corros. Sci. 134 (2018) 131–139.
[23] S. Alvi, D.M. Jarzabek, M.G. Kohan, D. Hedman, P. Jenczyk, M. Natile, A. Vomiero, F. Akhtar, ACS Appl. Mater. Interfaces 12 (2020) 21070–21079.
[24] N.A. Khan, B. Akhavan, H.R. Zhou, L. Chang, Y. Wang, L.X. Sun, M.M. Bilek, Z.W. Liu, Appl. Surf. Sci. 495 (2019) 143560.
[25] Y.S. Kim, H.J. Park, S.C. Mun, E. Jumaev, S.H. Hong, G. Song, J.T. Kim, Y.K. Park, K.S. Kim, S. Jeong, Y.H. Kwon, K.B. Kim, J. Alloys Compd. 797 (2019) 834–841.
[26] N.A. Khan, B. Akhavan, C.F. Zhou, L. Chang, Y. Wang, L.X. Sun, M.M. Bilek, Z.W. Liu, Surf. Coat. Technol. 402 (2020) 126327.
[27] L.Q. Chen, W. Li, P. Liu, K. Zhang, F.C. Ma, X.H. Chen, H.L. Zhou, X.K. Liu, Vacuum 181 (2020) 109706.
[28] P.P. Cui, W. Li, P. Liu, K. Zhang, F.C. Ma, X.H. Chen, R. Feng, P.K. Liaw, J. Alloys Compd. 834 (2020) 155063.
[29] A.D. Pogrebnjak, I.V. Yakushchenko, A.A. Bagdasaryan, O.V. Bondar, R. Krause-Rehberg, G. Abadias, P. Chartier, K. Oyoshi, Y. Takeda, V.M. Beresnev, O.V. Sobol, Mater. Chem. Phys. 147 (2014) 1079–1091.
[30] R. Chen, Z.B. Cai, J.B. Pu, Z.Y. Lu, S.Y. Chen, S.J. Zheng, C. Zeng, J. Alloys Compd. 827 (2020) 153836.
[31] H.T. Hsueh, W.J. Shen, M.H. Tsai, J.W. Yeh, Surf. Coat. Technol. 206 (2012) 4106–4112.
[32] X.G. Feng, K.F. Zhang, Y.G. Zheng, H. Zhou, Z.H. Wan, Mater. Chem. Phys. 239 (2020) 121991.
[33] B. Ren, S.Q. Yan, R.F. Zhao, Z.X. Liu, Surf. Coat. Technol. 235 (2013) 764–772.
[34] Z.C. Chang, S.C. Liang, S. Han, Y.K. Chen, F.S. Shieu, Nucl. Instrum. Methods Phys. B 268 (2010) 2504–2509.
[35] F. Rovere, D. Music, S. Ershov, M. Baben, H.G. Fuss, P.H. Mayrhofer, J.M. Schneider, J. Phys. D: Appl. Phys. 43 (2010) 035302.
[36] S.M. Wang, X.H. Yu, J.Z. Zhang, L.P. Wang, K. Leinenweber, D. He, Y.S. Zhao, Cryst. Growth Des. 16 (2016) 351–358.
[37] M. Adamik, P.B. Barna, I. Tomov, Thin Solid Films 317 (1998) 64–68.
[38] D.C. Tsai, Z.C. Chang, B.H. Kuo, M.H. Shiao, S.Y. Chang, F.S. Shieu, Appl. Surf. Sci. 282 (2013) 789–797.
[39] C.H. Lai, S.J. Lin, J.W. Yeh, S.Y. Chang, Surf. Coat. Technol. 201 (2006) 3275–3280.
[40] D.C. Tsai, Y.L. Huang, S.R. Lin, S.C. Liang, F.S. Shieu, Appl. Surf. Sci. 257 (2010) 1361–1367.
[41] P.K. Huang, J.W. Yeh, Surf. Coat. Technol. 203 (2009) 1891–1896.
[42] Y. Zhang, Y.J. Zhou, J.P. Lin, G.L. Chen, P.K. Liaw, Adv. Eng. Mater. 10 (2008) 534–538.
[43] J.W. Yeh, S.K. Chen, S.J. Lin, J.Y. Gan, T.S. Chin, T.T. Shun, C.H. Tsau, S.Y. Chang, Adv. Eng. Mater. 6 (2004) 299–303.
[44] Y. Zhang, X.H. Yan, W.B. Liao, K. Zhang, Entropy 20 (2018) 624–635.
[45] L. Karlsson, L. Hultman, J.E. Sundgren, Thin Solid Films 371 (2000) 167–177.
[46] S. Suresha, R. Gunda, V. Jayaram, J. Mater. Res. 22 (2007) 3501–3506.
[47] Y. Niu, J. Wei, Z. Yu, Surf. Coat. Technol. 275 (2015) 332–340.
[48] Y.Q. Fu, F. Zhou, Q.Z. Wang, M.D. Zhang, Z.F. Zhou, L. Kwork, Y. Li, J. Alloys Compd. 791 (2019) 800–813.
[49] S.J. Zheng, Z.B. Cai, J.B. Pu, C. Zeng, S.Y. Chen, R. Chen, L.P. Wang, Appl. Surf. Sci. 483 (2019) 870–874.
[50] J. Ding, L. Zhang, M.U. Lu, J. Wang, Z.B. Wen, W.H. Hao, Appl. Surf. Sci. 289 (2014) 33–41.
[51] S.J. Zheng, Z.B. Cai, J.B. Pu, C. Zeng, L.P. Wang, Appl. Surf. Sci. 483 (2021) 148520.
[52] J. Dai, H. Feng, H.B. Li, Z.H. Jiang, H. Li, S.C. Zhang, P. Zhou, T. Zhang, Corros. Sci. 174 (2020) 108792.
[53] R. Bayón, A. Igartua, J.J. González, U.R.D. Gopegui, Tribol. Int. 88 (2015) 115–125.
[54] Y.X. Wang, J.W. Zhang, S.G. Zhou, Y.C. Wang, C.T. Wang, Y.X. Wang, Y.F. Sui, J.B. Lan, Q.J. Xue, Appl. Surf. Sci. 528 (2020) 147061.
[55] Y. Sun, E. Haruman, Corros. Sci. 53 (2011) 4131–4140.
[56] J.P. Celis, P. Ponthiaux, F. Wenger, Wear 261 (2006) 939–946.
[57] Y.Q. Fu, F. Zhou, Q.Z. Wang, M.D. Zhang, Z.F. Zhou, Corros. Sci. 165 (2020) 108385.
[58] A. Hatem, J.L. Lin, R.H. Wei, R.D. Torres, C. Laurindo, G.B.D. Souza, P. Soares, Surf. Coat. Technol. 347 (2018) 1–12.
[59] A. López-Ortega, R. Bayón, J.L. Arana, Surf. Coating. Technol. 349 (2018) 1083–1097.
[60] X. Dai, M. Wen, K.K. Huang, X. Wang, L.N. Yang, J. Wang, K. Zhang, Appl. Surf. Sci. 447 (2018) 886–893.